The construction of nanotubular Ni-Mg phyllosilicate solid solution catalyst for boosting CO_2 catalytic conversion: Identifying the species variations and interactions

Dehui Wang [a], Jia Liu [a], Hai Li [a], Qing Liu [a,*], Yu Cheng [b,*], Xing Fan [a,*], Peng Liang [a,*]

[a] *Key Laboratory of Low Carbon Energy and Chemical Engineering, Shandong University of Science and Technology, Qingdao 266590, China*
[b] *College of Transportation, Shandong University of Science and Technology, Qingdao 266590, China*

A R T I C L E   I N F O

A B S T R A C T

Addressing the problems of easy collapse, Ni sintering and low catalytic activity over the nanotubular nickel phyllosilicate catalyst, the Mg species was doped *via* a simple hydrothermal method to construct the nanotubular Ni-Mg bimetallic phyllosilicate solid solution. The high thermal stability, nonreducible property and strong basicity of magnesium species led to the enhancement of anti-collapse, Ni-sintering resistance and basicity. As a result, the fine Ni particles and enhanced H_2 and CO_2 chemisorption and activation properties resulted in boosting the catalytic activity of both CO_2 methanation and CH_4-CO_2 reforming reactions. The Ni/Mg ratios and the reduction temperatures were detailed optimized, and the 600^oC-reduced Ni_8Mg_2-NT catalyst with the Ni/Mg ratio of 8:2 was the optimal, which also exhibited high long-term stability. In short, the formed Ni-Mg-phyllosilicate solid solution structure and the special interactions of different species brought about high catalytic performance of the nanotubular Ni-Mg phyllosilicate catalyst.

1. Introduction

Over the last few decades, massive CO_2 emissions deriving from the fossil fuels consumption have led to serious environmental problems including global warming [1], ocean acidification, as well as extreme climate change [2,3], which made the sustainable development of the economy and environment at high risk and even threatened human survival [4]. Catalytic conversion of CO_2 to the valuable chemicals is an important form to utilize CO_2 as a resource [5], among which CO_2 methanation and CH_4-CO_2 reforming have drawn much attention due to the obtaining methane or syngas with high efficiency [6]. The two reactions should be performed in the presence of a catalyst; coincidently, the nickel-based catalysts are active for the both reactions, because of the requirement of the similar catalytic active centers deriving from metallic Ni [7,8]. Furthermore, the two reactions are usually performed at high temperatures for economic reasons, together with the existence of hydrocarbon, the potential sintering of nickel particles and deposited carbon are the challenges for these catalysts [9].

Ni-phyllosilicate is a layered silicate consisting of continuous Si−O tetrahedral structural units alternating with octahedral structural units consisting of nickel oxide or hydroxide [10], which can be converted to

Ni/SiO_2 after reduction. The strong metal-support interaction originated from nickel phyllosilicate is the obvious advantage of the obtained Ni/SiO_2 catalyst compared with the conventional one prepared by precipitation or impregnation method [11]. Thus, Ni-phyllosilicate has been widely used in various catalytic reactions operated at high temperatures. For instance, Yang et al. synthesized Ni-phyllosilicate on the surface of SiO_2 microspheres by the evaporative ammonia method and obtained high resistance to sintering and coking in the partial oxidative reforming reaction of CH_4 [12]. Kong et al. used silica sol and nickel nitrate as precursors to produce Ni nanoparticle-embedded nickel phyllosilicate catalysts by the evaporative ammonia method, which showed high low-temperature activity (130 −150 ^oC) in the hydrogenolysis reaction of 5-hydroxymethylfurfural [13]. Authors also reported that the unreduced nickel phyllosilicate species could provide the Lewis acid center. Das et al. prepared CeO_2-modified nickel phyllosilicate catalysts with a sandwich-like structure using silica nanospheres as a template, and this domain-limited structure and the auxiliary effect of CeO_2 allowed the catalysts to be stable at 600 ^oC for 72 h with excellent resistance to carbon deposition for the dry reforming reaction of biogas [14].

Although different types of nickel phyllosilicate have been widely

---

studied, the morphology of nickel phyllosilicate also produce an important effect on the catalytic performance. Different from the conventional layered Ni-phyllosilicate, the nanotubular nickel phyllosilicate obtains the special morphology with the characteristics of low mass transfer resistance, which can also improve the reaction rate of the catalyst to a certain extent. In addition, the unique nanotubule-like structure can increase the specific surface area resulting in the high Ni dispersion after reduction. Guo et al. designed a series of nickel phyllosilicate nanotube catalysts, in which the interfacial reaction between CeO2 and phyllosilicate produced a large number of extrinsic defects as the active sites for methane dry reforming [15]. Although the tubular nickel phyllosilicate has displayed many advantages and been used in different fields, it also suffered from the problems of easy collapse and Ni sintering leading to the poor catalytic activity especially for the reactions carried out at high temperatures including CO_2 methanation [16] and CH_4-CO_2 reforming [17]. Therefore, the modification of the tubular nickel phyllosilicate to improve the anti-collapse and anti-sintering properties is in urgent need.

As one of the key components of a heterogeneous catalyst, the promoter can change the interaction between active components and the coordination environment, and enhance the chemisorption and activation of reactant molecules, resulting in the improved catalytic performance [18–20]. MgO is a widely used structure promoter [21], and its strong basicity is a promising advantage for CO_2 chemisorption and activation [22–24]. Jing et al. proposed the Ni-MgO/SiO2 catalysts with adjustable Ni particle size for CH_4-CO_2 reforming with high coking resistance [25]. Additionally, the Ni-SiO2-MgO catalyst with high basicity exhibited the high structural stability and good catalytic activity for reforming reactions [21]. The Ni/MgO catalysts with different Ni/Mg ratio were synthesized by coprecipitation method for sorbitol hydrolysis tests, whose activity was closely related to the Ni surface area and alkalinity deriving from MgO [26]. Zhao et al. reported that synergistic interaction of MgO and NiO nanoparticles over the Ni-MgO/MAS-24 catalyst made the Ni particles highly dispersed and effectively prevented coking and aggregation of the active species [27]. In addition, the multicore-shell Ni-Mg phyllosilicate nanotubes@silica catalyst was synthesized with high activity for CH_4-CO_2 reforming, where the silica shell helped to enhance the thermal stability and suppress coking formation [28]. In summary, the addition of Mg species is a reasonable strategy to boost the activity and stability of the catalyst especially for the reactions with CO_2 as raw material.

In this work, a group of tubular nickel-magnesium bimetallic phyllosilicate catalysts were synthesized, which were tuned with different Ni/Mg ratios (Ni-NT, Ni8Mg2-NT, Ni5Mg5-NT, Ni2Mg8-NT, Mg-NT) and evaluated for both CO_2 methanation and CH_4-CO_2 reforming reactions. The reduction temperature was also investigated to further improve the catalytic activity, and the results showed that the Ni8Mg2-NT catalyst reduced at 600 °C was the most competitive one. In order to reveal the Mg species variation during the synthesis, calcination and reduction process as well as the interaction between Mg species and Ni active centers, various tests and characterizations were performed, which were shown in the following sections.

2. Experimental section

2.1. Materials

All materials including chemicals and gases were displayed in Appendix A. Supplementary data in detail.

2.2. Synthesis of nanotubular Ni phyllosilicate

The nanotubular nickel or/and magnesium phyllosilicates were prepared using a hydrothermal method (Fig. 1), and the experimental parameters and naming rule were shown in Table 1 and Table S1, respectively.

Typically, Ni(NO3)2·6 H2O (1.16 g, 4 mmol) was added in the deionized water (60.0 mL) to form a green transparent solution. A sodium silicate solution (0.5 mol·L^{-1}, 8.0 mL) was added to the above solution under stirring, and the light green precipitate was formed. After the further stirring for 10 min, NaOH (6.00 g, 0.15 mol) was added to the above mixture, which was treated in an autoclave at 200 °C for 24 h. Finally, the sample was collected after centrifugation, washing, and air drying at 80 °C for 10 h, and referred to as "Ni-NT", in which "NT" stood for "nanotubular phyllosilicate".

2.3. Synthesis of nanotubular Ni-Mg bimetallic phyllosilicate

The nanotubular Ni-Mg bimetallic phyllosilicates with different Ni/Mg ratio were synthesized using the same procedures with Ni-NT except for the addition of Ni(NO3)2·6 H2O (0.93 g, 3.2 mmol) together with the certain amount of Mg(NO3)2·6 H2O (Table 1). The obtained products were referred to as "NixMgy-NT", in which x/y was the molar ratio of Ni/Mg with the values of 8/2, 5/5 and 2/8. Here, the Ni content of the as-synthesized Ni-NT, Ni8Mg2-NT, Ni5Mg5-NT and Ni2Mg8-NT measured by ICP was 46.26, 34.83, 24.74 and 10.12 wt% , respectively (Table 1).

2.4. Synthesis of nanotubular magnesium phyllosilicate

The procedures of the preparation of nanotubular magnesium phyllosilicate were almost the same with those of Ni-NT except for the addition of Mg(NO3)2·6 H2O (1.02 g, 4 mmol) rather than Ni(NO3)2·6 H2O. The obtained product was referred to as "Mg-NT".

Table 1
Experimental parameters for the preparation of Ni-NT, NixMgy-NT (x/y = 8/2, 5/5 and 2/8) and Mg-NT.

Samples	Ni (NO3)2·6 H2O (mmol)	Mg (NO3)2·6 H2O (mmol)	Na2SiO3 (mL)[a]	NaOH (mol)	Ni content (wt%)[b]
Ni-NT	4.0	—	8.0	0.15	46.26
Ni8Mg2-NT	3.2	0.8	8.0	0.15	34.83
Ni5Mg5-NT	2.0	2.0	8.0	0.15	24.74
Ni2Mg8-NT	0.8	3.2	8.0	0.15	10.12
Mg-NT	—	4.0	8.0	0.15	—

[a] Na2SiO3·9 H2O aqueous solution of 0.5 mol·L^{-1}.
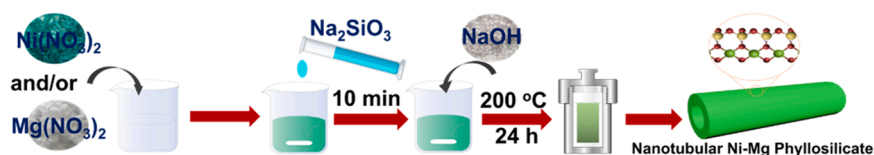[b] Ni content, determined by ICP.

Fig. 1. Schematic diagram of the typical catalyst synthesis using a hydrothermal method.

2.5. Characterizations

The characterizations including inductively coupled plasma atomic emission spectrometry (ICP), X-ray diffraction (XRD) analysis, scanning electron microscope (SEM) and transmission electron microscope (TEM) observations, N_2 sorption, Fourier-transform infrared spectra (FT-IR), H_2 temperature programmed reduction (H_2-TPR), H_2 temperature programmed desorption (H_2-TPD), CO_2 temperature programmed desorption (CO_2-TPD), active surface area (S_m), Ni dispersion (D) measurement, X-ray photoelectron-spectrometer (XPS), and *in situ* diffuse reflectance infrared Fourier transform spectroscopy (*in situ* DRIFTS) were displayed in Appendix A. Supplementary data in detail.

2.6. Catalytic performance measurements

The catalytic tests procedures including catalytic activities for CO_2 methanation and CH_4-CO_2 reforming, activation energy (E_a), turnover frequency (TOF) measurements, and long-term stability were shown in Appendix A. Supplementary data in detail.

3. Results

3.1. Catalytic activity test

Firstly, the four 700°C-reduced Ni-phyllosilicate-based catalysts were evaluated for CO_2 methanation. In Fig. 2a–c, the CO_2 conversion of Ni-NT showed a volcanic trend with the maximum at around 450 °C. As well known, CO_2 methanation reaction was strongly exothermic, and high temperatures were not conducive to this reaction according to Le Chatelier's principle. Interestingly, the three Ni_xMg_y-NT catalysts showed the similar change rule with Ni-NT. In addition, the CH_4 selectivity of Ni_xMg_y-NT was relatively close with each other, which was higher than that of Ni-NT. The only by-product detected by gas chromatography was CO originated from the reverse water gas shift reaction. Among them, Ni_8Mg_2-NT was the best with the maximum CO_2 conversion of 72.5% and CH_4 yield of 72.1% at 450 °C, followed by Ni_5Mg_5-NT > Ni-NT > Ni_2Mg_8-NT (Fig. 2a–c and Fig. S1a). Apparently, compared with Ni/NT, the construction of nanotubular Ni-Mg bimetallic phyllosilicate with the appropriate Ni/Mg ratio could improve the catalytic activity. For Ni_2Mg_8-NT, the lowest Ni content should be the main reason for the worst catalytic activity [29]. However, the CO_2 conversion could not reach the thermodynamics equilibrium curve in the whole temperature range, indicating the catalytic activity of the 700 °C-reduced catalyst was relatively low.

In order to further boost the catalytic activity, the reduction temperature of 600 °C was also investigated. Here, only the three catalysts of Ni-NT, Ni_8Mg_2-NT and Ni_5Mg_5-NT with good performance were selected for evaluation. For the three 600 °C-reduced catalysts, the catalytic activity followed similar volcanic trends to those of the 700 °C-reduced catalysts (Fig. 2d–e). Significantly, the higher catalytic performance was obtained; in detail, the CO_2 conversion of Ni_8Mg_2-NT could reach thermodynamics equilibrium at 450 °C, and its CH_4 selectivity almost reached the thermodynamics equilibrium from the initial temperature of 300 °C and exceeded the equilibrium curve due to the control of both thermodynamics and dynamics at high temperatures. As a result, at 450 °C, Ni_8Mg_2-NT, which was reduced at 600 °C, showed a maximum CO_2 conversion of 78.8% and CH_4 yield of 77.2%. In addition, the catalytic performance of other catalysts also increased, indicating that the low temperature reduction led to higher catalytic activity.

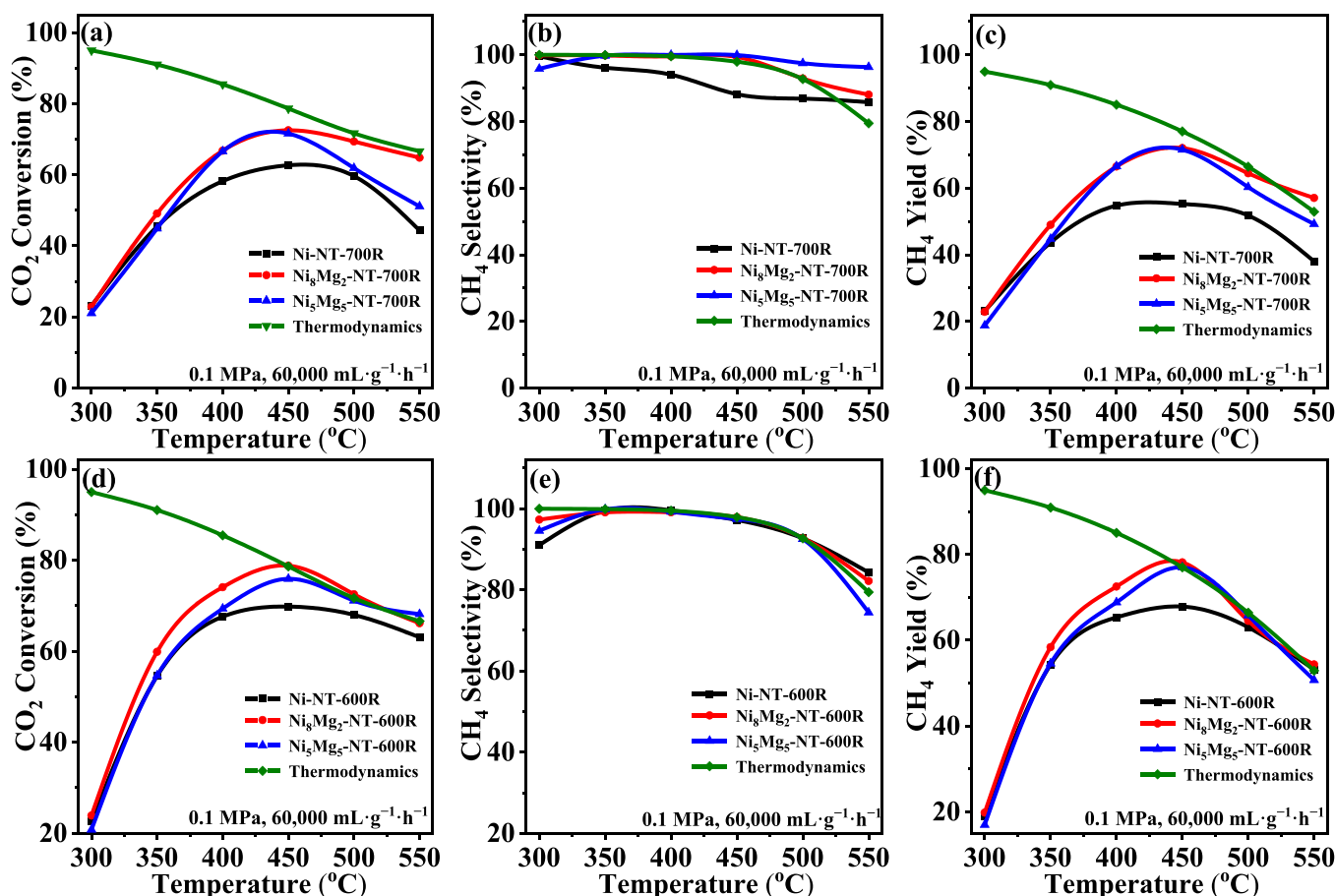On the contrary, the activities of the three 500 °C-reduced catalysts

Fig. 2. Catalyst activity of the 700 or 600°C-reduced catalysts for CO_2 methanation: (a and d) CO_2 conversion, (b and e) CH_4 selectivity, and (c and f) CH_4 yield.

were all very low because of the low reduction degree (Fig. S1b). Surprisingly, the CH_4 selectivity was also decreased compared with that of 700 or 600 °C-reduced catalyst (Fig. S1c); as a result, the CH_4 yield was also very low (Fig. S1d). Despite all this, Ni_8Mg_2-NT was the best among the three 500 °C-reduced catalysts. Furthermore, these catalysts were also reduced at 400 °C for 1 h; unfortunately, the 400 °C-reduced catalysts were inactive for CO_2 methanation because of the too low reduction temperature (data not shown here). At the same time, the CO selectivity of all samples was shown in Fig. S1e. Apparently, the above results indicated that reduction temperature was an important parameter for investigation of catalytic activity, and 600 °C was the optimal value in this work.

Furthermore, the three catalysts (Ni-NT, Ni_8Mg_2-NT and Ni_5Mg_5-NT) were also reduced at the optimal temperature of 600 °C and evaluated for CH_4-CO_2 reforming (Fig. 3). This was an endothermic reaction and the catalytic performance of the three catalysts including the conversion of CO_2 and CH_4, H_2 selectivity as well as H_2 yield increased in the operation temperature range of 550 − 800 °C. Overall, Ni_8Mg_2-NT was still the best with the maximum CO_2 conversion of 95.8%, CH_4 conversion of 97.9%, and H_2 yield of 97.9% at 800 °C, followed by Ni_5Mg_5-NT, and Ni-NT was the worst. To sum up, combined with the above evaluation results, Ni_8Mg_2-NT exhibited the best catalytic performance for both CO_2 methanation and CH_4-CO_2 reforming reactions in this work.

3.2. X-ray diffraction analysis

The as-synthesized Ni-NT catalyst showed diffraction peaks corresponding to $Ni_3Si_2O_5(OH)_4$ (JCPDS No. 20–0791) (Fig. 4a) [30], suggesting that sodium silicate and nickel nitrate had completely converted to nickel phyllosilicate after the hydrothermal treatment at 200 °C for 24 h. After the doping of Mg species, the XRD diffraction patterns of Ni_8Mg_2-NT, Ni_5Mg_5-NT and Ni_2Mg_8-NT (shown in Fig. S2b) were almost the same with that of Ni-NT. There might be two existence states of Mg species: the one was in the form of magnesium phyllosilicate to construct the mixture of Ni-phyllosilicate and Mg-phyllosilicate; the other was in the form of Ni-Mg phyllosilicates solid solution with high Mg dispersion [31]. In order to investigate the two possibilities, the as-synthesized Mg-NT sample was also analyzed and it showed the similar diffraction peaks corresponding to $Mg_3Si_2O_5(OH)_4$ (JCPDS No. 27–1275). Therefore, it was reasonable that the five samples above with the different components obtained the similar crystalline phase structure with the ratio of SiO_4 tetrahedron to M-O(OH) octahedron (M = Ni and/or Mg coordinated to six O atoms or OH groups) of 1:1. After the careful matching with the PDF card, it was found that Ni_xMg_y-NT belonged to Ni-Mg phyllosilicates solid solution with the formula of $[Ni_{1-x}Mg_x]_3(OH)_4Si_2O_5 \cdot zH_2O$, which was also a metal phyllosilicate with 1:1 type. In short, Ni-Mg phyllosilicates should be in the state of solid solution rather than physical mixture of Ni-phyllosilicate and Mg-phyllosilicate (Fig. S2c).

As mentioned in Figs. 2 and 3 as well as Fig. S1, the different reduction temperature could affect the catalytic performance; thus, the
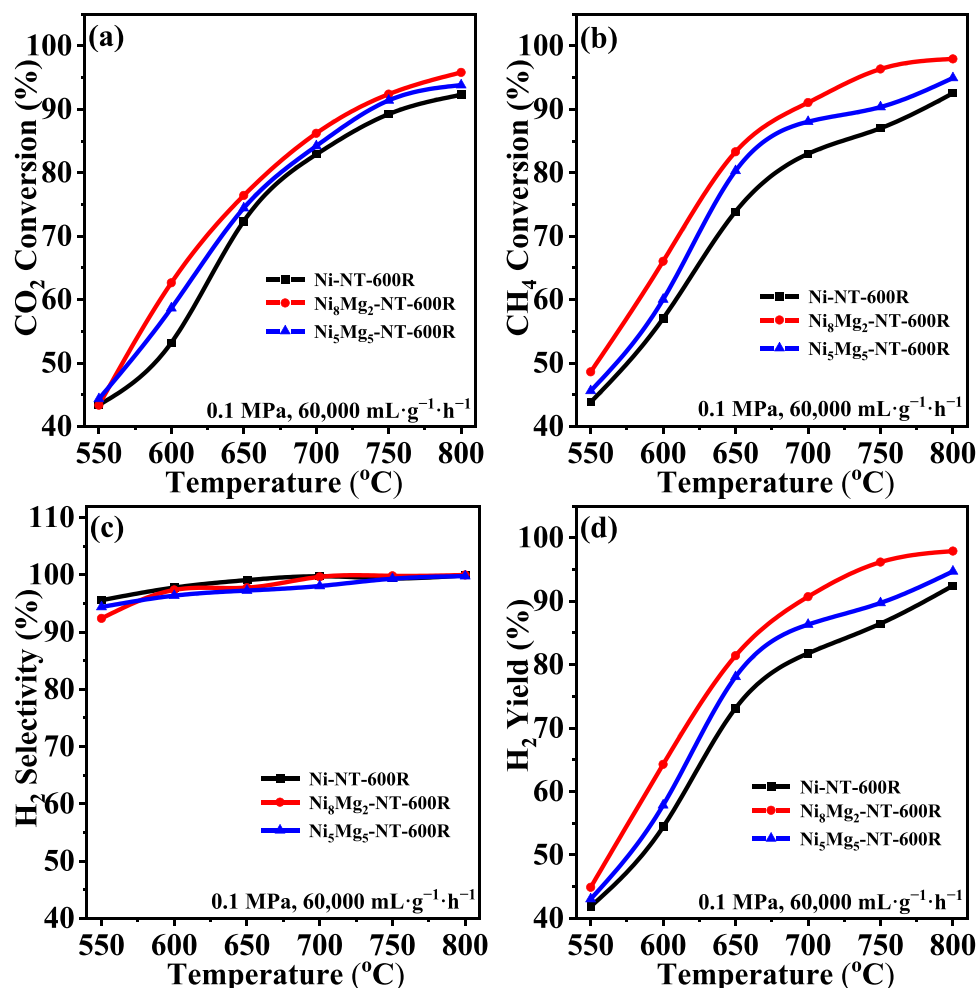

Fig. 3. Catalyst activity of the 600°C-reduced catalysts for CH_4-CO_2 reforming: (a) CO_2 conversion, (b) CH_4 conversion, (c) H_2 selectivity, and (d) H_2 yield.
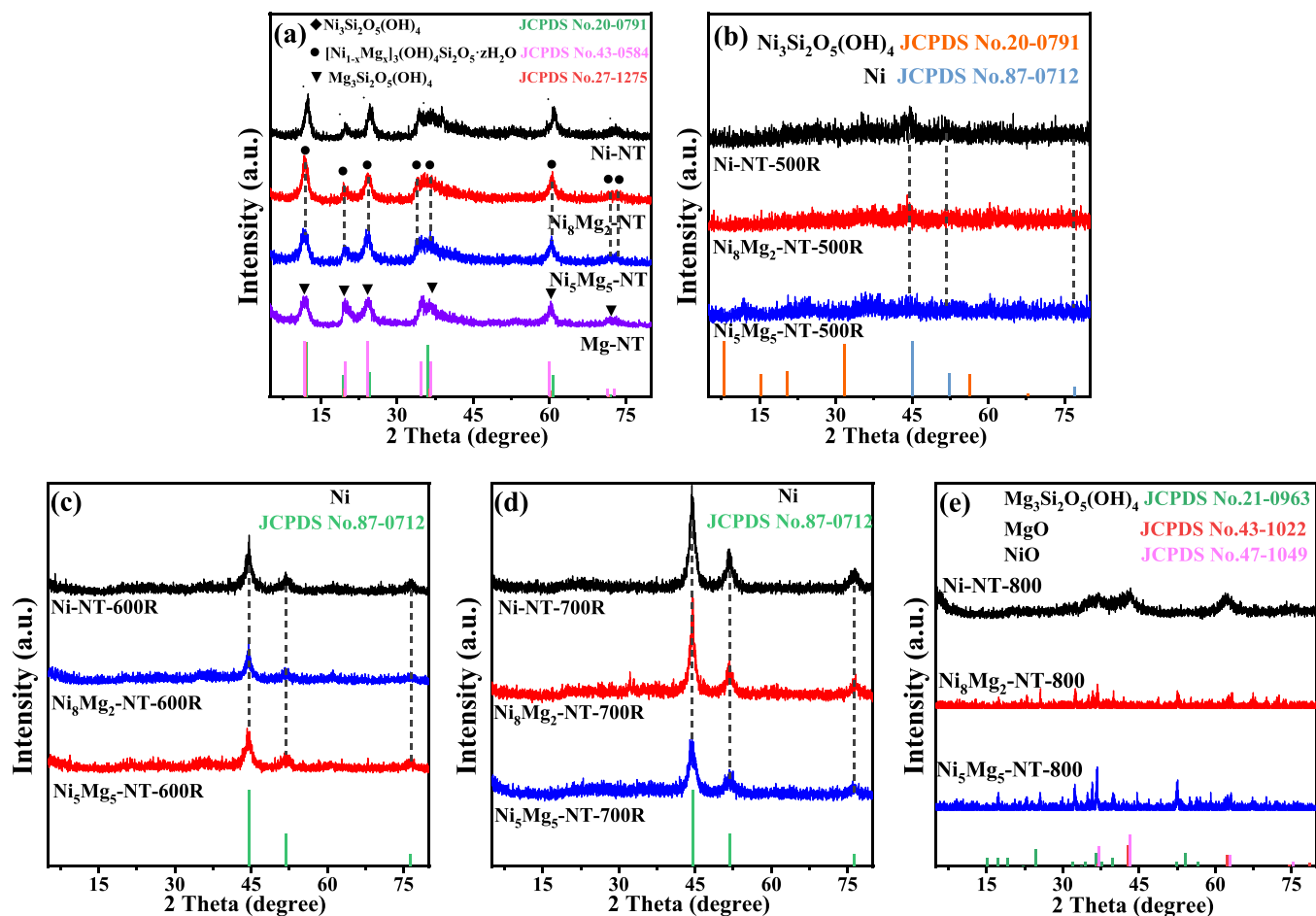
Fig. 4. XRD patterns: (a) the as-synthesized catalysts, (b) the 500°C-reduced catalysts, (c) the 600°C-reduced catalysts, (d) the 700°C-reduced catalysts, (e) the 800°C-calcined catalysts.

reduced Ni-NT, Ni$_8$Mg$_2$-NT, and Ni$_5$Mg$_5$-NT catalysts at 500, 600 and 700 °C were also analyzed by XRD. Surprisingly, after the reduction at 500 °C, the diffraction peaks attributing to Ni-phyllosilicate disappeared, and a tiny peak occurred at 44.4° on the XRD pattern of 500°C-reduced Ni-NT belonging to metallic Ni (JCPDS No. 87–0712) (Fig. 4b). On the contrary, there was no obvious diffraction peak attributing to Ni-phyllosilicate over the 500°C-reduced Ni$_8$Mg$_2$-NT and Ni$_5$Mg$_5$-NT, and the peaks of metallic Ni could also not be identified. After the reduction at 600 °C, the three diffraction peaks were obviously observed on the all samples, which were attributed to the metallic nickel (Fig. 4c) [26]. Similar with Fig. 4b, there was no peak attributing to metal phyllosilicate or Mg species. Furthermore, for the 700 °C-reduced samples, the similar three diffraction peaks with stronger intensity were observed attributing to Ni (Fig. 4d) [26]. It was noteworthy that these diffraction peaks became sharper and narrower as the reduction temperature increased, suggesting the increase of the Ni crystal size. It was a great pity that the Ni crystal size could not be calculated in Fig. 4b due to the too weak peaks. As expected, the nickel crystal size of the three 600°C-reduced catalysts was 4.84, 4.17, and 4.01 nm, respectively; while that of the three 700°C-reduced catalysts was 5.01, 4.73, and 4.35 nm (Table 2 and Table S2). It was apparent that the overreduction of a catalyst at high temperature led to further growth of Ni particle size resulting in decrease of catalyst activity.

In order to further investigate the change of crystal phase with the increase of reduction temperature, Ni$_8$Mg$_2$-NT was picked out as a representative, and the XRD patterns of the as-synthesized as well as the 400, 500, 600 and 700°C-reduced Ni$_8$Mg$_2$-NT were shown in Fig. S2a. The XRD pattern of 400°C-reduced Ni$_8$Mg$_2$-NT was almost the same with

Table 2
Physical and chemical properties of samples.

Samples	Ni crystal size (nm)[a]	Ni particle size (nm)[b]	S_{BET} (m²·g⁻¹)[c]	V_P (cm³·g⁻¹)[d]	D (nm)[e]
Ni$_8$Mg$_2$-NT-400R	—	—	136	0.49	11.56
Ni$_8$Mg$_2$-NT-500R	—	2.61	—	—	—
Ni-NT-600R	4.84	5.12	87	0.41	12.36
Ni$_8$Mg$_2$-NT-600R	4.17	4.78	112	0.44	12.61
Ni$_5$Mg$_5$-NT-600R	4.01	4.23	108	0.48	18.03

[a] Calculated by the XRD diffraction peak ($2\theta = 44.4°$) using the Debye-Scherrer equation.
[b] Estimated from the TEM images.
[c] S_{BET}, surface area, derived from the BET equation.
[d] V_P, pore volume, obtained from the volume of nitrogen adsorbed at the relative pressure of 0.97.
[e] D, average pore diameter, derived from BET equation.

the as-synthesized one, indicating that 400 °C was too low to reduce Ni-NT to metallic Ni. A nearly unrecognizable peak occurred at around 44.4° on the XRD pattern of 500°C-reduced Ni$_8$Mg$_2$-NT attributing to the (111) crystal plane of the metallic Ni, indicating that the metallic nickel with very small size was reduced from Ni$_8$Mg$_2$-NT at 500 °C. As the reduction temperature increased, the diffraction peaks belonging to the metallic Ni became higher and narrower, signifying the increase of the Ni crystal size.

It was very strange that, in Fig. 4b–d and Fig. S2a, no diffraction peaks attributing to Mg phyllosilicate or MgO were found on the XRD patterns of the reduced samples even at the high Mg species content. To

further reveal the variation of Mg species, the as-synthesized Ni-NT, Ni_8Mg_2-NT, Ni_5Mg_5-NT, and Mg-NT were calcined at 800 °C in air. Interestingly, on the XRD pattern of the Ni-NT catalyst after the calcination at 800 °C, the diffraction peaks of Ni-phyllosilicate disappear and new peaks attributing to NiO with low intensity could be seen (Fig. 4e), indicating that the tubular Ni phyllosilicate was decomposed to NiO and the amorphous silica. For the XRD patterns of Ni_8Mg_2-NT and Ni_5Mg_5-NT after the calcination at 800 °C, the peak intensity also decreased compared with the as-synthesized ones in Fig. 4a. MgO (JCPDS No. 43–1022) as well as NiO (JCPDS No. 47–1049) together with magnesium phyllosilicate (JCPDS No. 21–0963) were observed over the 800°C-calcined Ni_8Mg_2-NT and Ni_5Mg_5-NT [32]. In addition, the intensities of Mg species increased with the increase of their contents. The above results showed that the nickel phyllosilicate completely decomposed to NiO and SiO_2, while magnesium phyllosilicate only partially decomposed at 800 °C in air, indicating its higher thermal stability compared with Ni-phyllosilicate. Moreover, the Mg species evolution varied with the operation atmosphere (H_2 or air), which could change its speciation as well as crystal state.

3.3. Morphology analysis

To visualize the morphology of the samples, the SEM images of the as-synthesized samples were shown in Fig. 5. Ni-NT showed a typical nanotube morphology, and the length of the tubes varied in a wide range with the outer diameter of around 25 nm (Fig. 5a), which was the excellent evidence of the successful preparation of nanotubular nickel phyllosilicate. At the same time, the as-synthesized Ni_8Mg_2-NT (Fig. 5b), Ni_5Mg_5-NT (Fig. 5c), Ni_2Mg_8-NT (Fig. S3) and Mg-NT (Fig. 5d) also showed the typical nanotube morphology, which indicated the doping of Mg species did not change the tubular structure. In addition, the length of Ni_xMg_y-NT and Mg-NT was also unregular, and some of them could be as long as 437 nm; meanwhile, their diameters were almost the same without varying with the composition.

In order to obtain the inner diameter and wall thickness information, the as-synthesized Ni_8Mg_2-NT catalyst was then observed by TEM (Fig. 6a–c). As expected, the typical tubular structure could be seen in Fig. 6a, whose inner and outer diameter was in the range of 11–12 and 23–25 nm, respectively (Fig. 6b), and the length of the tube could be 321 nm. In addition, the typical cross-sections of nanotubes were spiral or concentric (Fig. 6c). As reported in the literature, the formed $Ni_3Si_2O_5(OH)_4$ nanosheets could be bent along the crystallographic [100] direction and the ends of the rolling sheets met to form a circumference of complete nanotubes during the hydrothermal process (Fig. 6c) [33].

Then, the TEM images of the 400, 500, 600 and 700°C-reduced Ni_8Mg_2-NT were recorded in Fig. 6d−g. After the reduction at 400 °C, Ni_8Mg_2-NT-400R (Fig. 6d) displayed the similar structure and morphology with the as-synthesized one (Fig. 6a–c). On the contrary, fine Ni particles highly dispersed on the nanotubes were observed over the 500°C-reduced Ni_8Mg_2-NT (Fig. 6e). As the reduction temperature increased, more and larger black dots could be seen on the TEM image of Ni_8Mg_2-NT after reduction at 600 °C, but the complete tubular structure could still be seen (Fig. 6f). When the reduction temperature reached 700 °C, the tubular morphology was hard to be identified with black dots fully covered the whole catalyst (Fig. 6g). The size of nickel particle size was estimated and that of the Ni_8Mg_2-NT reduced at 500, 600 and 700 °C was 2.61, 4.78 and 5.09 nm respectively (Table 2 and Table S4). Apparently, the high reduction temperature led to the large nickel particle size. In addition, the reduced Ni-NT and Ni_5Mg_5-NT at 600 and 700 °C were also recorded by TEM (Figs. 6g and 6h as well as Fig. S4), which exhibited the similar morphology with the reduced Ni_8Mg_2-NT in Figs. 6f and 6g. The average nickel particle sizes of these catalysts were estimated; in detail, that of the 600 °C-reduced Ni-NT and Ni_5Mg_5-NT catalysts was 5.12 and 4.23 nm, respectively; and those reduced at 700 °C were 5.38 and 4.65 nm (Table 2 and Table S2). Apparently, the doping of Mg species could be conducive to reduce the Ni particle size, and higher Mg content led to smaller Ni particle size owing to its physical barrier effect during reduction process.

Moreover, the elemental distribution was recorded by the dark-field TEM and elemental mapping. For the 600 °C-reduced Ni_8Mg_2-NT, the bright spots corresponded the Ni particles in Figs. 7a and 7b; and Ni, Mg,

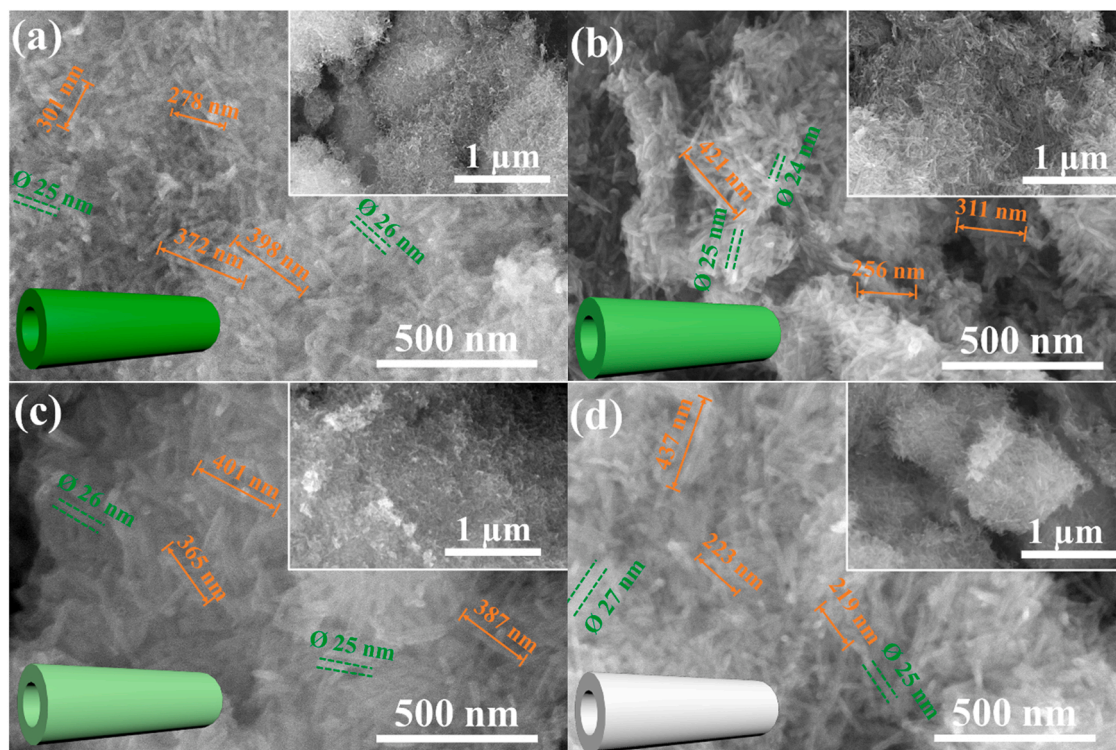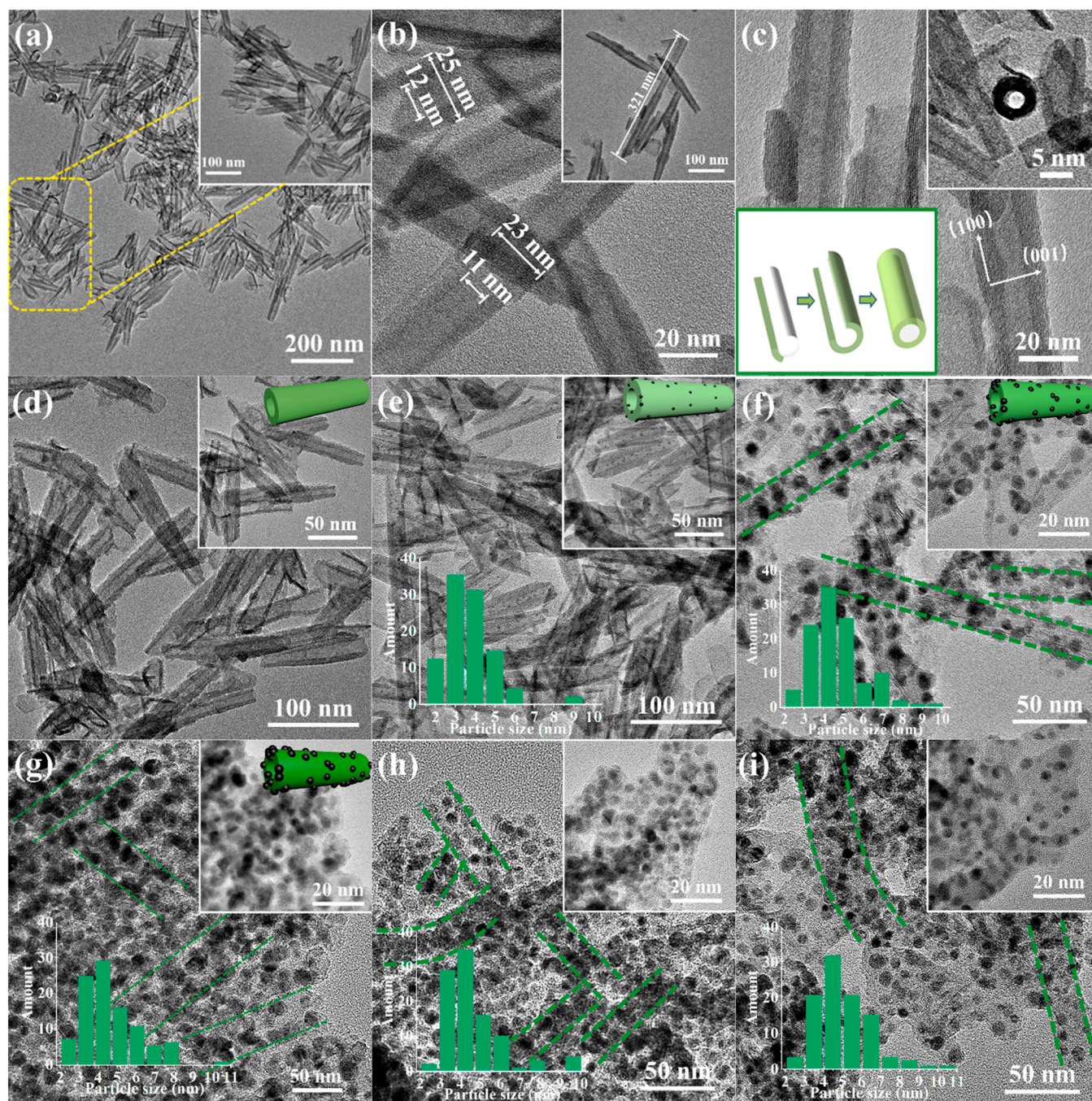**Fig. 5.** SEM images of the as-synthesized samples: (a) Ni-NT, (b) Ni_8Mg_2-NT, (c) Ni_5Mg_5-NT, (d) Mg-NT.

Fig. 6. TEM images of Ni_8Mg_2-NT: (a–c) the as-synthesized, (d) 400^oC-reduced, (e) 500^oC-reduced, (f) 600^oC-reduced, and (g) 700^oC-reduced; TEM images of the 700^oC-reduced Ni-NT (h), and Ni_5Mg_5-NT (i).

O, and Si were uniformly dispersed throughout the catalyst (Fig. 7c−f). As expected, the peaks of Ni and Mg were clearly visible through the EDS analysis (Fig. 7g). In addition, it was observed from the HRTEM images in Fig. 7h that the lattice spacing of around 0.20 nm belonging to the Ni (111) crystal plane could be clearly seen.

Combined with the above results, the variations of Ni-NT and Ni_8Mg_2-NT during the reduction and 800^oC-calcination processes were displayed in Fig. 7i. For Ni-NT, the Ni-phyllosilicate ($Ni_3Si_2O_5(OH)_4$) was formed during the synthesis process and converted to Ni/SiO_2 after the reduction above $500\ ^oC$. It was noted that the tubular structure was also destroyed during the high-temperature reduction at $700\ ^oC$. Meanwhile, the thermal stability of Ni-NT was poor, which completely decomposed to NiO and the amorphous silica after the calcination at

$800\ ^oC$. On the contrary, for Ni-Mg-NT, the Ni-Mg phyllosilicates ($[Ni_{1−x}Mg_x](OH)_4Si_2O_5 \bullet zH_2O$) solid solution was formed rather than the physical mixture of $Ni_3Si_2O_5(OH)_4$ and $Ni_3Si_2O_5(OH)_4$. During the reduction process, the Ni species showed the similar change with that in Ni-NT, and the metallic Ni could be observed above $500\ ^oC$; however, no diffraction peaks attributing to Mg phyllosilicate or MgO were found on the XRD patterns of the reduced samples (500, 600 and $700\ ^oC$), indicating the crystal state might convert to the amorphous in the H_2 flow. Surprisingly, MgO and NiO together with magnesium phyllosilicate (JCPDS No. 21–0963) were observed over the 800^oC-calcined Ni_8Mg_2-NT. Apparently, nickel-magnesium phyllosilicate only partially decomposed during the calcination process at $800\ ^oC$ in air. In short, the variation of Ni species in Ni-NT and Ni_8Mg_2-NT was the same; while that
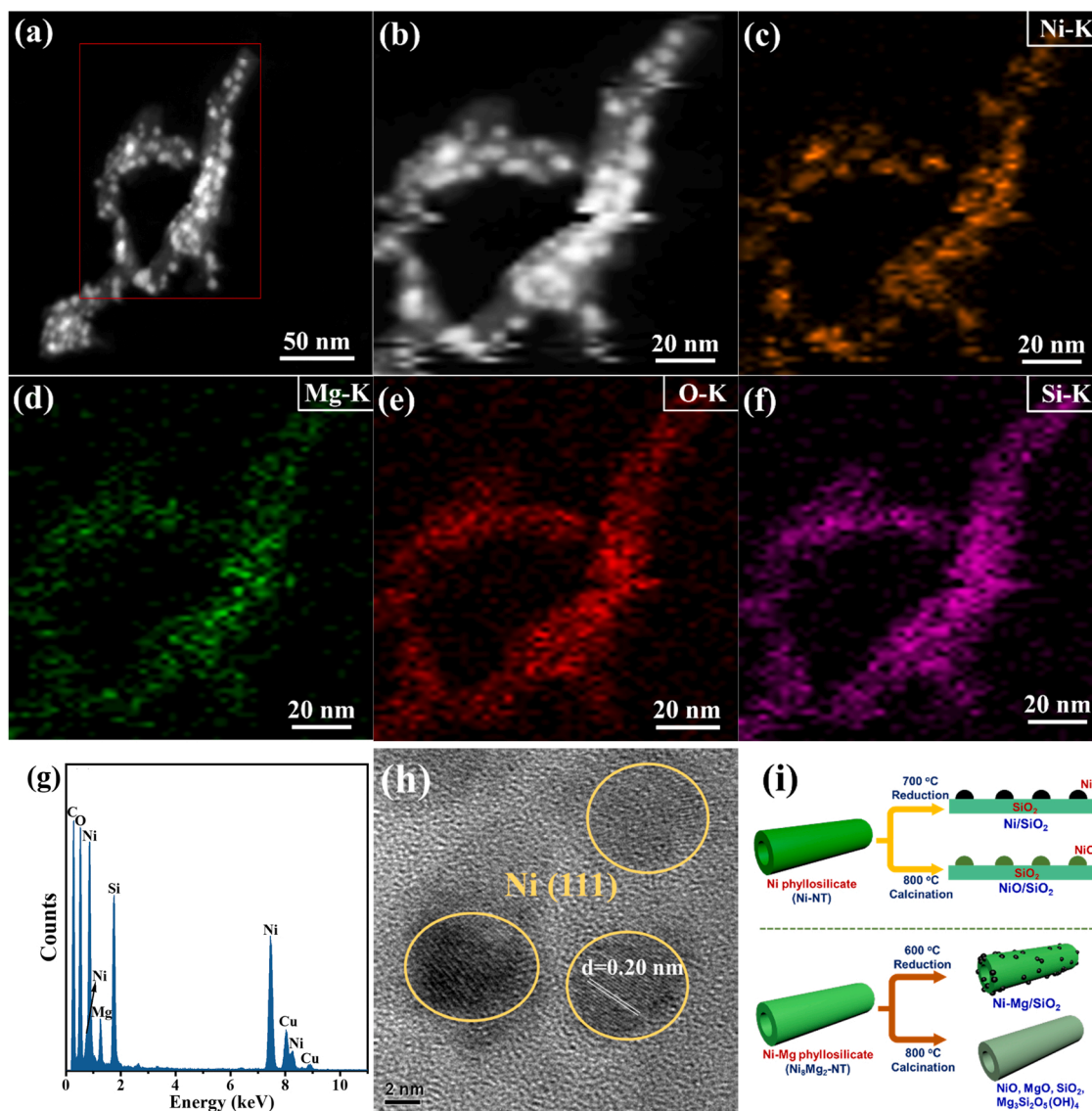
Fig. 7. HAADF-STEM images (a and b) of the 600 °C-reduced Ni_8Mg_2-NT, and elemental maps of Ni (c), Mg (d), O (e), Si (f); EDS analysis (g), HRTEM image of the 600 °C-reduced Ni_8Mg_2-NT (h), and diagram of Ni-NT and Ni_8Mg_2-NT variations during the reduction and 800°C-calcination processes (i).

of Mg species was different, which varied with the thermal treatment atmosphere (H_2 or air).

3.4. N_2 sorption and FT-IR analyses

In Fig. 8a, the as-synthesized Ni-NT catalyst showed isotherms of type IV with hysteresis loop of H3 between P/P_0 of $0.5 - 0.97$, indicating that the tubular nickel phyllosilicate was a typically mesoporous material. Compared to Ni-NT, the adsorption-desorption isotherms of N_xM_y-NT were almost unchanged, suggesting that the addition different amounts of Mg species had little influence on the pore structure (Fig. 8a and S5a). For Mg-NT, the adsorption-desorption isotherms were still isotherms of type IV with hysteresis loop of H3 between P/P_0 of $0.5 - 0.97$, which was also a typical mesoporous material. Furthermore, for the as-synthesized Ni-NT, the peak of the pore size distribution (PSD) curve was concentrated around 15 nm (Fig. 8b), which coincided with the TEM observation of the inner diameter. The PSD curves also showed some changes with increase of Mg species; in detail, higher Mg content led to larger pore size. The specific surface areas (S_{BET}) and pore volumes (V_P) as well as the average pore diameter (D_P) of the different as-synthesized catalysts also increased with the increase of Mg content in

Table 3. However, for the three samples (Ni-NT, Ni_5Mg_5-NT and Ni_5Mg_5-NT) reduced at 600 °C, the S_{BET} were significantly reduced owing to the partial destruction of pores during the reduction process (Table 2); as a result, there was also some changes for their adsorption-desorption isotherms (Figs. 8c and 8d). Significantly, the obvious changes were observed over the isotherms and the PSD curve of the 600°C-reduced Ni-NT compared with the as-synthesized one, due to the relatively poor stability and high content of Ni-phyllosilicate.

Next, the functional groups of the as-synthesized Ni-NT and Ni_8Mg_2-NT were also analyzed by FT-IR spectra to reveal the effect of Mg species doping (Fig. S5b). For Ni-NT, the peak at 1093 cm^{-1} corresponded to the bending and stretching vibrations of the Si−O−Si bond, while the peaks at 3460 and 1630 cm^{-1} belonged to the stretching and bending vibrations of O−H. Significantly, δ-OH band was also observed at around 670 cm^{-1}, which was the characteristic peak of metal phyllosilicate of 1:1 type [16]. After doping of Mg species, the FT-IR spectrum of Ni_8Mg_2-NT was almost consistent with that of Ni-NT, indicating the modification did not obviously change the functional groups.

In order to detailed investigate the change of pore structure with different reduction temperatures, Ni_8Mg_2-NT was selected as the representative, which was reduced at 400, 500 and 600 °C, respectively
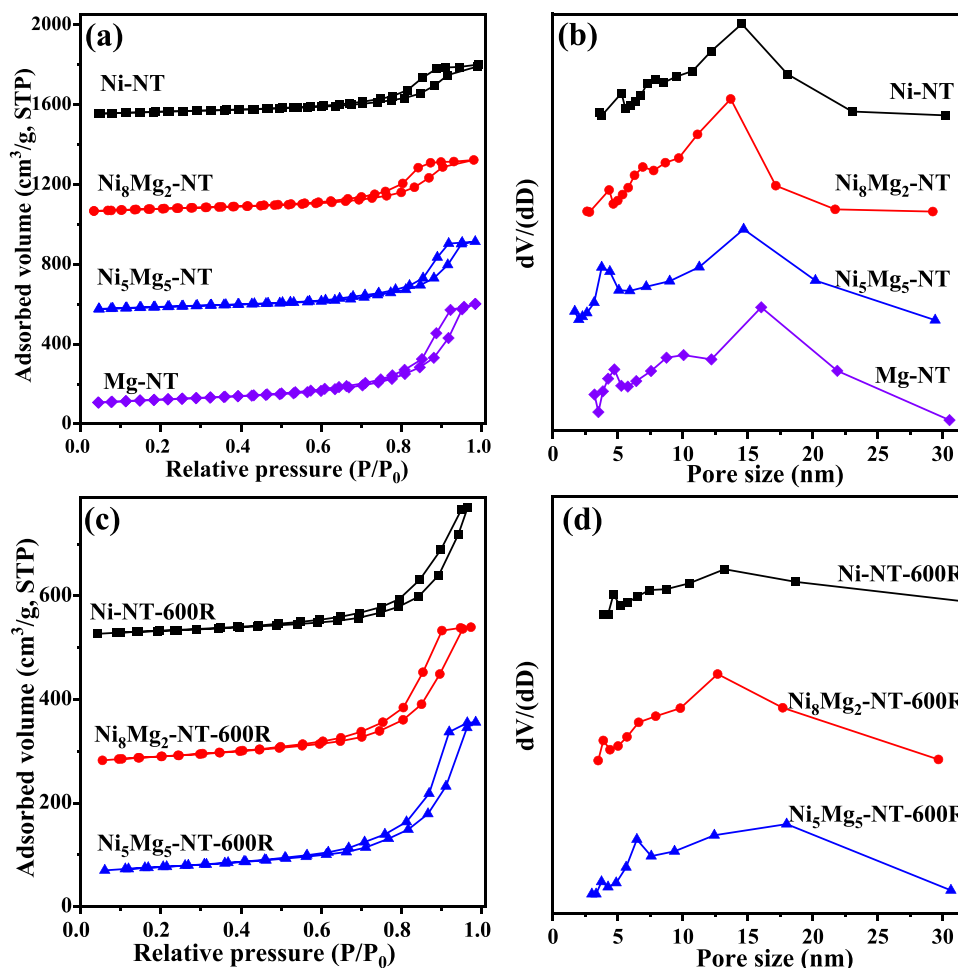
Fig. 8. N$_2$ adsorption isotherm (a) and the pore size distribution curve (b) of the as-synthesized catalysts; N$_2$ adsorption isotherm (c) and the pore size distribution curve (d) of 600°C-reduced catalysts.

Table 3
Pore structure parameters of the as-synthesized samples.

Samples	S_{BET} (m$^2\cdot$g^{-1})[a]	V_P (cm$^3\cdot$g^{-1})[b]	D_P (nm)[c]
Ni-NT	123	0.40	10.72
Ni$_8$Mg$_2$-NT	137	0.41	10.19
Ni$_5$Mg$_5$-NT	145	0.54	13.48
Mg-NT	203	0.80	13.45

[a] S_{BET}, surface area, derived from the BET equation.
[b] V_P, pore volume, obtained from the volume of nitrogen adsorbed at the relative pressure of 0.97.
[c] D_P, average pore diameter, derived from BET equation.

(Fig. S5c and S5d). There was only slight change of the adsorption-desorption isotherms (Fig. S5c) and the PSD curve almost remained unchanged with different treatment (Fig. S5d), indicating the stability of the tubular structure of Ni$_8$Mg$_2$-NT. Moreover, the decrease of S_{BET} and slight increase of D_P pore were also observed with the increase of reduction temperature (Tables 2 and 3).

3.5. Chemisorption analysis

On the H$_2$-TPR profile of Ni-NT, the single H$_2$ consumption peak was in the range of 400 − 900 °C, which centered at around 700 °C (Fig. 9a). For Ni$_8$Mg$_2$-NT and Ni$_5$Mg$_5$-NT, two H$_2$ consumption peaks at 670 and 774 or 802 °C were observed, attributing to the reduction of nickel species in the Ni-Mg phyllosilicate [12]. Meanwhile, for the peak at

670 °C, the shift towards the low-temperature region after the doping of magnesium species was because the reduction difficulty of the surface Ni phyllosilicate was alleviated [12,21]. On the contrary, the H$_2$ consumption peak at 700 − 800 °C was attributed to Ni phyllosilicate covered by the Mg phyllosilicate, which increased the reduction difficulty of nickel species [21]. Significantly, the integral areas of the peaks in Fig. 9a were directly proportional to their Ni contents in Table 1. For Mg-NT, the absence of the H$_2$ consumption peak indicated that Mg^{2+} species could not be reduced to metallic Mg.

Next, the H$_2$-TPR analysis of the Ni$_8$Mg$_2$-NT catalyst after reduction at 400, 600, and 700 °C was carried out. For the catalyst reduced at 400 °C, only a single H$_2$ consumption peak appeared at around 680 °C. Apparently, the high temperature contributed to the reduction of Ni-phyllosilicate [34], which was consistent with the XRD result in Fig. 4a. In contrast, on the H$_2$-TPR profiles of the catalysts reduced at 600 and 700 °C, two H$_2$ consumption peaks appeared in the range of 100 − 300 °C. The one located in the low-temperature region (158 or 168 °C) was attributed to the fine NiO particles; the one centered at 254 or 274 °C should correspond to large NiO particles inside the bulk [35]. In addition, the Ni reduction degrees of the three samples were also calculated, which was in the order of 10.1% (Ni$_8$Mg$_2$-NT-400R) < 96.6% (Ni$_8$Mg$_2$-NT-600R) < 98.2% (Ni$_8$Mg$_2$-NT-700R). Combined with the results in Fig. 2 and Fig. S1b−d, it was seen that high Ni reduction degree could not lead to high catalytic activity, and the reasons would be analyzed in the Discussion section in detail.

Fig. 9c showed the H$_2$-TPD profile of the Ni-NT, Ni$_8$Mg$_2$-NT and Ni$_5$Mg$_5$-NT catalysts reduced at 600 °C. Overall, there was only one H$_2$
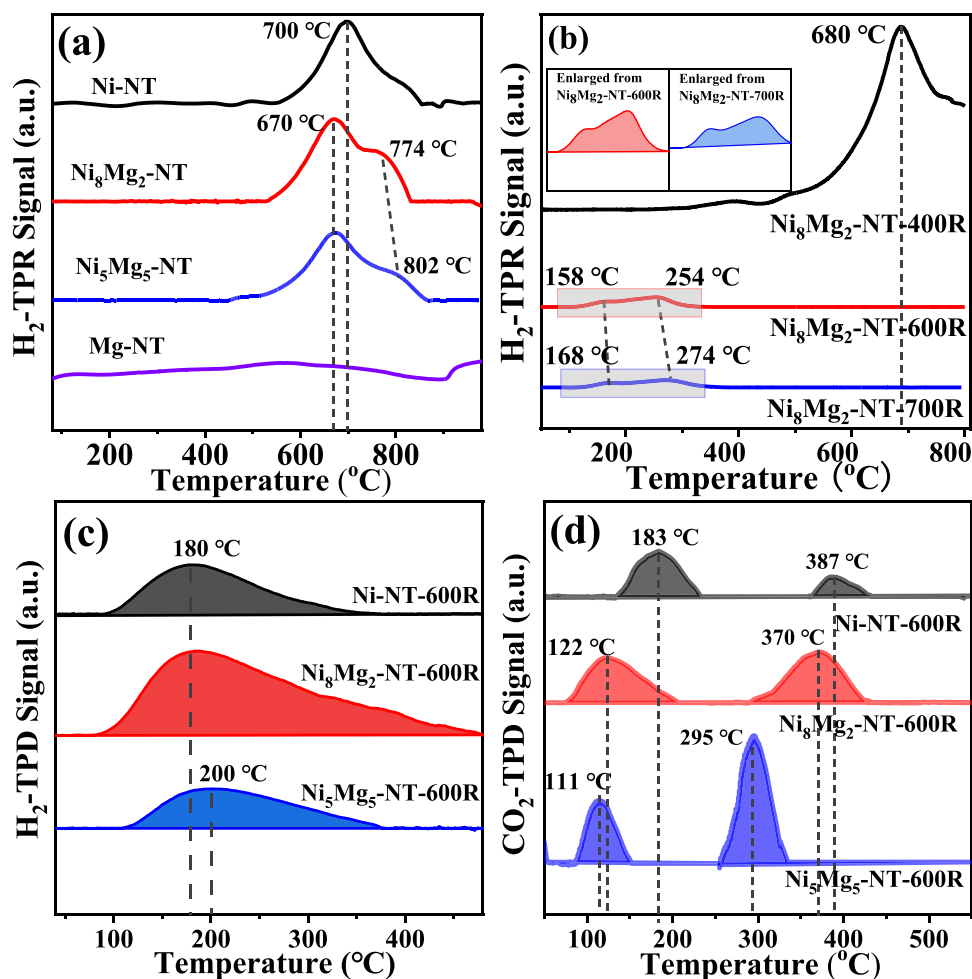
Fig. 9. H_2-TPR profiles of as-synthesized catalysts (a) and Ni_8Mg_2-NT reduced at different temperatures (b), H_2-TPD (c) and CO_2-TPD profiles (d) of the 600°C-reduced catalysts.

desorption peak centered in the range of $180 - 200$ °C. This was attributed to the adsorption of hydrogen from the highly dispersed Ni nanoparticles [36]. Interestingly, although with the lower Ni content, the peak area of Ni_8Mg_2-NT was much larger than that of Ni-NT owing to its much smaller Ni particle size. In addition, the small peak area of Ni_5Mg_5-NT derived from its low Ni content. In all, the H_2 uptakes of the catalysts followed the sequence of Ni_8Mg_2-NT (425.4 µmol·g^{-1}) > Ni_5Mg_5-NT (357.6 µmol·g^{-1}) > Ni_5Mg_5-NT (255.6 µmol·g^{-1}). Furthermore, the calculated Ni dispersion of Ni-NT, Ni_8Mg_2-NT, and Ni_5Mg_5-NT was 8.1%, 16.5%, and 10.3%, respectively (Table 4), indicating that the addition of an appropriate amount of Mg species was conducive to improving the dispersion of Ni. Meanwhile, the active surface areas (S_m) of the 600 °C-reduced Ni-NT, Ni_8Mg_2-NT, and

Ni_5Mg_5-NT were also calculated, which was 5.2, 19.1, and 12.5 m^2·g^{-1}, respectively (Table 4). Generally, the high Ni dispersion and S_m could result in the high catalytic activity, which might be the reason for the best catalytic performance in Fig. 2 and Fig. 3.

In Fig. 9d, the CO_2-TPD profiles of the three catalysts displayed two CO_2 desorption peaks. The peak in the range of $110 - 183$ °C attributed to the weak basic site on the catalyst surface with the monodentate coordination of CO_2 [37]; while the other peak belonged to the moderate basic site with the bidentate coordination of CO_2 [37,38]. Interestingly, the peaks of the weak and moderate basic sites both shifted to low temperature as the increase of Mg species content, indicating more Mg species could reduce the activation difficulty of CO_2. Inexplicably, the peak areas of the CO_2-TPD profiles of Ni_8Mg_2-NT and Ni_5Mg_5-NT were similar, which were much larger than that of Ni-NT. In all, the doping of Mg species led to enhancement of both CO_2 adsorption and activation capacity.

3.6. XPS analysis

Fig. 10a showed the wide XPS spectra of the three 600°C-reduced catalysts. Besides the peaks of Ni, Si and O, the peak of the Mg 1 s was also seen over Ni_8Mg_2-NT and Ni_5Mg_5-NT. Moreover, the peak intensities of Mg species (around 1305.3 and 307.3 eV) were directly proportional to the Mg content. For the Ni $2p_{3/2}$ XPS spectra, the bonding energy of Ni^0 of the three reduced Ni-NT, Ni_8Mg_2-NT, and Ni_5Mg_5-NT catalysts was the same of 852.6 eV, suggesting that the Mg modification did not alter the electronic environment of metallic Ni

Table 4
H_2 uptake, Ni dispersion, active surface area and TOF of the 600°C-reduced catalysts.

Samples	H_2 uptake (µmol·g^{-1})[a]	D[b] (%)	S_m[c] (m^2·g^{-1})	TOF$_{CO_2}$ 220 °C (s^{-1})[d]
Ni-NT	255.6	8.1	5.2	1.09×10^{-3}
Ni_8Mg_2-NT	425.4	16.5	19.1	2.98×10^{-3}
Ni_5Mg_5-NT	357.6	10.3	12.5	2.89×10^{-3}

[a] H_2 uptake, calculated based on the H_2-TPR and H_2-TPD results.
[b] Ni dispersion, calculated from the H_2-TPR and H_2-TPD results.
[c] Active surface area
[d] Turnover frequency, calculated based on the metal dispersion and the CO_2 conversion at 220 °C.
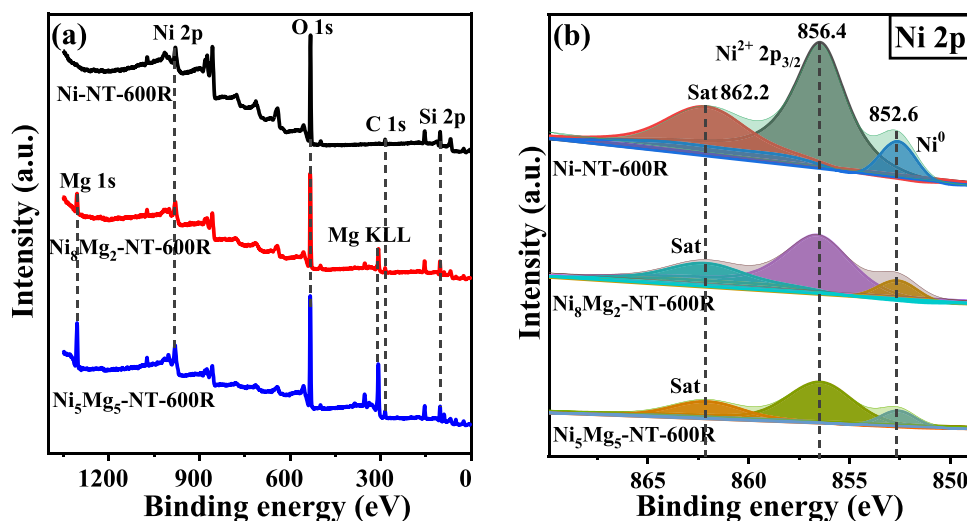
Fig. 10. Wide XPS spectra (a) and Ni 2p spectra (b) of the 600°C-reduced catalysts.

(Fig. 10b). Furthermore, the peaks of 856.4 eV and 862.2 eV on the Ni $2p_{3/2}$ spectra were attributed to Ni^{2+}. As mentioned above, the reduction degree of Ni_8Mg_2-NT-600R was 96.6%; thus, the Ni^{2+} species in Fig. 10b was derived from the oxidization of metallic Ni in air as well as the unreduced Ni-phyllosilicate species [39].

3.7. Long-term stability test

To study the long-term stability of the optimal Ni_8Mg_2-NT catalyst, an operating temperature of 450 °C was chosen for the 100-h test of CO_2 methanation. Meanwhile, Ni-NT was also evaluated as the reference. Both the 600°C-reduced Ni-NT and Ni_8Mg_2-NT catalysts did not reach thermodynamic equilibrium at 450 °C, and the change of the catalyst surface structure was sensitive with its catalytic activity. As shown in Fig. 11, the CO_2 conversion decreased by approximately 1.4% for Ni_8Mg_2-NT and 1.8% for Ni-NT. The CH_4 selectivity decreased by approximately 0.2% for Ni_8Mg_2-NT and 0.4% for Ni-NT. After the test, the spent catalysts were characterized by XRD and TEM (Fig. S6). The nickel crystal size of the spent Ni-NT increased to 5.41 nm (Fig. S6a) with the average Ni particle size of 5.87 nm (Fig. S6b); at the same time, the nickel particle size of the spent Ni_8Mg_2-NT was 5.24 nm (Fig. S6c) with the Ni crystal size of 4.92 nm (Fig. S6d). Apparently, Ni_8Mg_2-NT exhibited the higher Ni sintering resistance. In short, the both Ni-NT and Ni_8Mg_2-NT catalyst displayed high long-term stability, and Ni_8Mg_2-NT

seemed to be much more stable than Ni-NT.

4. Discussion

4.1. Effect of Ni/Mg ratio and reduction temperature

As mentioned in Fig. 2 and Fig. S1, both Ni/Mg ratio and reduction temperature played a significant role in boosting the catalytic activity. As shown in Fig. 12, the nanotubular materials could be successfully formed with the Ni/Mg ratio varying from 10:0–0:10, whose color changed with the component; while the crystal phase was still 1:1 type phyllosilicate with the formula of $M_3Si_2O_5(OH)_4$ (M=Ni or Mg). However, the Ni content as well as Mg doping were both important for the catalytic activity, which followed the sequence of Ni_8Mg_2-NT > Ni_5Mg_5-NT > Ni-NT > Ni_2Mg_8-NT at the reduction temperature of 700 °C for CO_2 methanation. Thus, the Ni/Mg ratio seemed to be more important than the Ni content. The formation of Ni-Mg phyllosilicate solid solution and the imitate contact with Ni species and Mg species could maximize the promotion effect, and Ni_8Mg_2-NT obtained higher catalytic activity compared with Ni-NT. Furthermore, the Ni/Mg ratio was closely related with the anti-collapse property. During the reduction process, Ni-phyllosilicate would convert to Ni/SiO_2 catalyst in H_2 flow resulting in the destruction and collapse of the tubular structure; however, the thermal stability and nonreducible property of Mg-phyllosilicate species
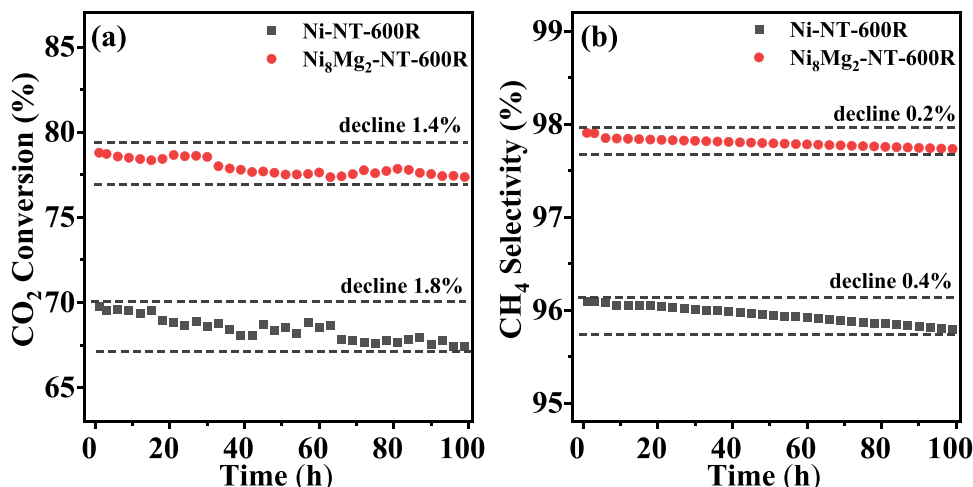

Fig. 11. Long-term stability test of the 600°C-reduced Ni-NT and Ni_8Mg_2-NT: (a) CO_2 conversion, and (b) CH_4 selectivity.
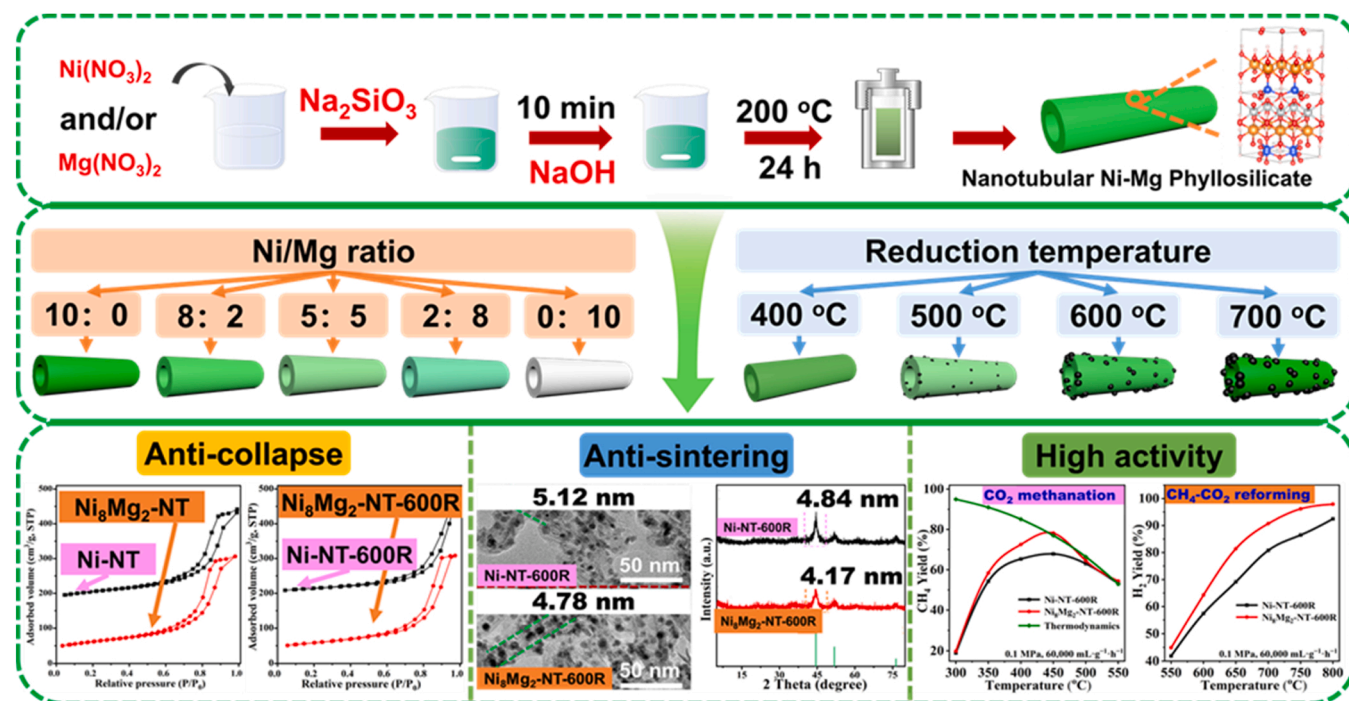
Fig. 12. Overview of the effect of Ni/Mg ratio and reduction temperature on physical and chemical properties of the nanotubular Ni-Mg bimetallic phyllosilicate.

could retain its original form to provide the support and physical barrier for Ni/SiO$_2$, leading to the enhancement of the anti-collapse of the nanotubes.

On the other hand, the stability and anti-collapse property could be maintained below a certain operation temperature, and the too high temperature was also the challenge for the Ni-Mg phyllosilicate materials. Thus, the reduction temperature was also optimized in this work, and 600 $^{\circ}$C was the optimal value. This was because the too high temperature (700 $^{\circ}$C) led to the serious collapse and the passivation of the active centers, and too low temperature (400 and 500 $^{\circ}$C) could not achieve the enough active Ni species. As a result, the optimal 600°C-reduced-Ni$_8$Mg$_2$-NT catalyst showed the highest CO$_2$ conversion compared to some reported CO$_2$ methanation catalysts in literature (Table S3). Meanwhile, this catalyst still exhibited the high CH$_4$ conversion for CH$_4$-CO$_2$ reforming (Table S4). In all, the modification of Mg species to for the nanotubular Ni-Mg phyllosilicate solid solution could improve the anti-collapse, anti-sintering and catalytic activity compared with the nanotubular Ni-phyllosilicate.

4.2. Kinetic analysis for CO$_2$ methanation

In order to further explore the effect of doped species Mg on catalytic performance, the kinetic analysis of the 600°C-reduced Ni-NT, Ni$_8$Mg$_2$-NT and Ni$_5$Mg$_5$-NT for CO$_2$ methanation was performed. In this test, CO$_2$ conversion was controlled to below 10% using different space velocities and operation temperatures (210, 220, and 230 $^{\circ}$C), and the activation energy (E_a) was calculated following the Arrhenius equation (Fig. 13). The order of E_a values for the three catalysts was Ni-NT (143.25 kJ·mol^{-1}) > Ni$_5$Mg$_5$-NT (103.26 kJ·mol^{-1}) > Ni$_8$Mg$_2$-NT (55.29 kJ·mol^{-1}). This result was in good agreement of the catalytic activity trend in Fig. 2. Furthermore, the calculated TOF$_{CO2}$ (220 $^{\circ}$C) values for Ni-NT, Ni$_8$Mg$_2$-NT and Ni$_5$Mg$_5$-NT were 1.09×10^{-3}, 2.98×10^{-3} and 2.89×10^{-3} s^{-1}, respectively (Table 4). The similar TOF$_{CO2}$ of Ni$_8$Mg$_2$-NT and Ni$_5$Mg$_5$-NT indicated that the intrinsic catalytic power of each active site was similar, and the different Ni content led to the different catalytic activity between them. On the other hand, the low TOF$_{CO2}$ of Ni-NT was the root cause for its low catalytic activity. In short, the addition of the species Mg had an important effect on the

both E_a and TOF$_{CO2}$ of the catalyst due to differences in nickel content, nickel particle size, and the chemisorption properties of H$_2$ and CO$_2$.

4.3. Reaction pathway and intermediate analysis by in-situ DRIFTS

To study the possible pathways and reaction intermediates of the CO$_2$ methanation reaction catalyzed by the Ni-NT and Ni$_8$Mg$_2$-NT catalysts, the in-situ DRIFTS analysis was performed (Fig. 14). For the spectra of Ni-NT in Fig. 13a, the absorption peaks around 3750 cm^{-1} belonged to the O−H stretching vibration of the Si−OH. Furthermore, the absorption peak intensity of the O−H stretching vibrations gradually increased as the temperature varied from 50 to 350 $^{\circ}$C, indicating a gradual increase in the amount of O−H with increasing temperature. This was derived from the formation of H$_2$O or OH in the CO$_2$ methanation reaction on the catalyst surface [40–42]. In addition, the peaks around 3010 and 1302 cm^{-1} attributing to C−H stretching vibration were also observed, which usually consisted of methylene (=CH−), methyl (CH$_3$ −), and −CH$_2$ − groups [43]. All of them were the key reaction intermediates in the hydrogenation of CO$_2$ to CH$_4$, and could provide the important evidence for the formation of CH$_4$. Significantly, in the enlarged view with the wavenumber range of 2960 − 3060 cm^{-1}, the C−H peak occurred from 225 $^{\circ}$C, which could be considered as its temperature for initiation of activity. Additionally, the observed peaks at 2390 and 2320 cm^{-1} corresponded to the adsorbed CO$_2$ molecule on the catalyst surface. Interestingly, the absorbance peaks at 1930 and 1830 cm^{-1} were observed above 150 $^{\circ}$C, which should be caused by the stretching vibration of the bridged CO molecule – one of the reaction intermediates for methanation of CO$_2$ [44]. Furthermore, the characteristic absorbance peak of monodentate HCOO$^-$ was located at 1580 cm^{-1}, indicating the CO$_2$ methanation reaction also underwent the reaction intermediate of HCOO$^-$ [45]. Similar with the peaks of CO, the HCOO$^-$ peak also occurred at 150 $^{\circ}$C, indicating the formation of intermediates of CO and HCOO$^-$ was synchronous.

On the other hand, the similar absorbance peaks could also be seen on the in-situ DRIFTS spectra of the 600°C-reduced Ni$_8$Mg$_2$-NT catalyst (Fig. 14b). It was worth noting that the two intermediates of CO and HCOO$^-$ occurred at a lower temperature of 125 $^{\circ}$C, and their peak intensities were also stronger than those of Ni-NT. Meanwhile, the
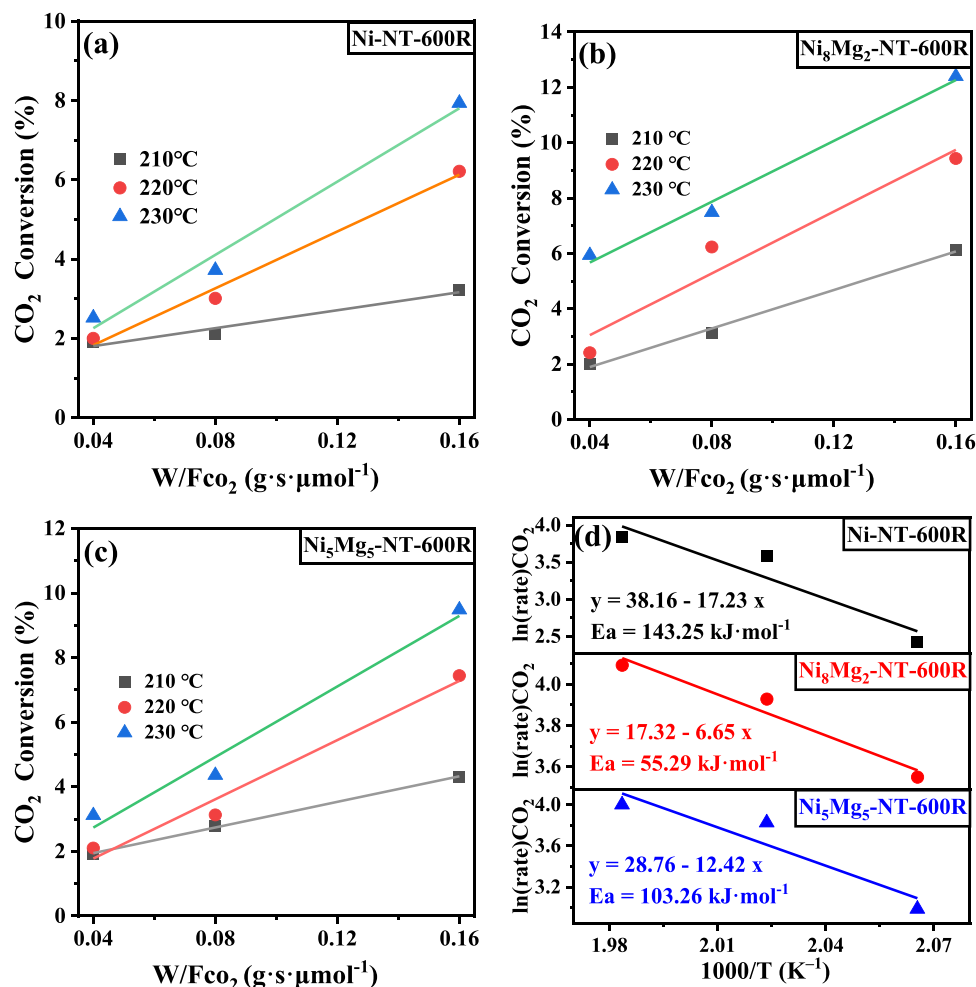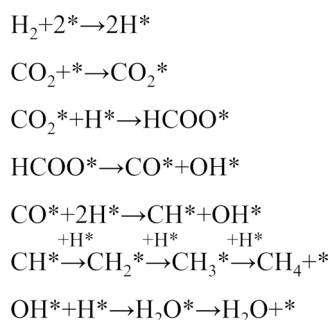
Fig. 13. Variation of CO_2 conversion of the 600^oC-reduced catalysts with W/F_{CO2}: (a) Ni-NT, (b) Ni_8Mg_2-NT, and (c) Ni_5Mg_5-NT; and Arrhenius plots for CO_2 methanation on different catalysts (d).

absorbance peak of C−H bond appeared at 200 ^oC with relatively strong intensity, which was also lower than that of Ni-NT. The above results indicated that the Ni_8Mg_2-NT catalyst possessed better low-temperature catalytic activity than Ni-NT. Finally, it was concluded that mono-dentate $HCOO^-$ and bridged CO were possible reaction intermediates for further hydrogenation to CH_x – species for the CO_2 methanation [41]. The reaction pathway inferred from *in-situ* DRIFTS was shown below:

$$H_2 + 2^* \rightarrow 2H^*$$

$$CO_2 + ^* \rightarrow CO_2^*$$

$$CO_2^* + H^* \rightarrow HCOO^*$$

$$HCOO^* \rightarrow CO^* + OH^*$$

$$CO^* + 2H^* \rightarrow CH^* + OH^*$$

$$CH^* \xrightarrow{+H^*} CH_2^* \xrightarrow{+H^*} CH_3^* \xrightarrow{+H^*} CH_4 + ^*$$

$$OH^* + H^* \rightarrow H_2O^* \rightarrow H_2O + ^*$$

.

5. Conclusions

To suppress the problems of easy collapse, Ni sintering and low catalytic activity of the nanotubular nickel phyllosilicate, a series of Mg-doped nanotubular nickel-magnesium phyllosilicate catalysts were prepared by a simple hydrothermal method, and evaluated for both CO_2 methanation and CH_4-CO_2 reforming reactions. In order to obtain the optimal catalyst, the Ni/Mg ratio as well as the reduction temperature were investigated, and the 600^oC-reduced Ni_8Mg_2-NT catalyst with Ni/Mg ratio of 8:2 showed high catalytic performance in CO_2 methanation with a CO_2 conversion of 78.8% and CH_4 selectivity of 99.1% at 450 ^oC, 0.1 MPa, 60000 mL·g^{-1}·h^{-1}, low E_a of 55.29 kJ·mol^{-1} and large TOF_{CO2} of 2.98×10^{-3} s^{-1} at 220 ^oC. *In situ* DRIFTS results displayed that CO and $HCOO^-$ were the key intermediates for hydrogenation of CO_2 to CH_4, and the occurrence of these intermediates and CH_x – species at lower temperature further testified the higher activity of Ni_8Mg_2-NT. Additionally, this catalyst also should high catalytic activity for CH_4-CO_2 reforming with the CO_2 conversion of 95.8% and CH_4 conversion of 97.9% at 800 ^oC, and high long-term stability for CO_2 methanation with excellent anti-sintering property. The characterization results showed that the formed nanotubular Ni-Mg bimetallic phyllosilicate was in the state of solid solution rather than physical mixture of Ni-phyllosilicate and Mg-phyllosilicate. The high thermal stability and nonreducible property of Mg-phyllosilicate species as well as its intimate contact with Ni-phyllosilicate resulted in the enhanced the anti-collapse and anti-sintering properties of the Ni-Mg phyllosilicate compared with the conventional tubular Ni-phyllosilicate. The decreased Ni particle size and increased H_2 and CO_2 chemisorption capacity resulted in the boosting catalytic performance. In all, the construction of the nano-tubular Ni-Mg bimetallic phyllosilicate could address the problems of
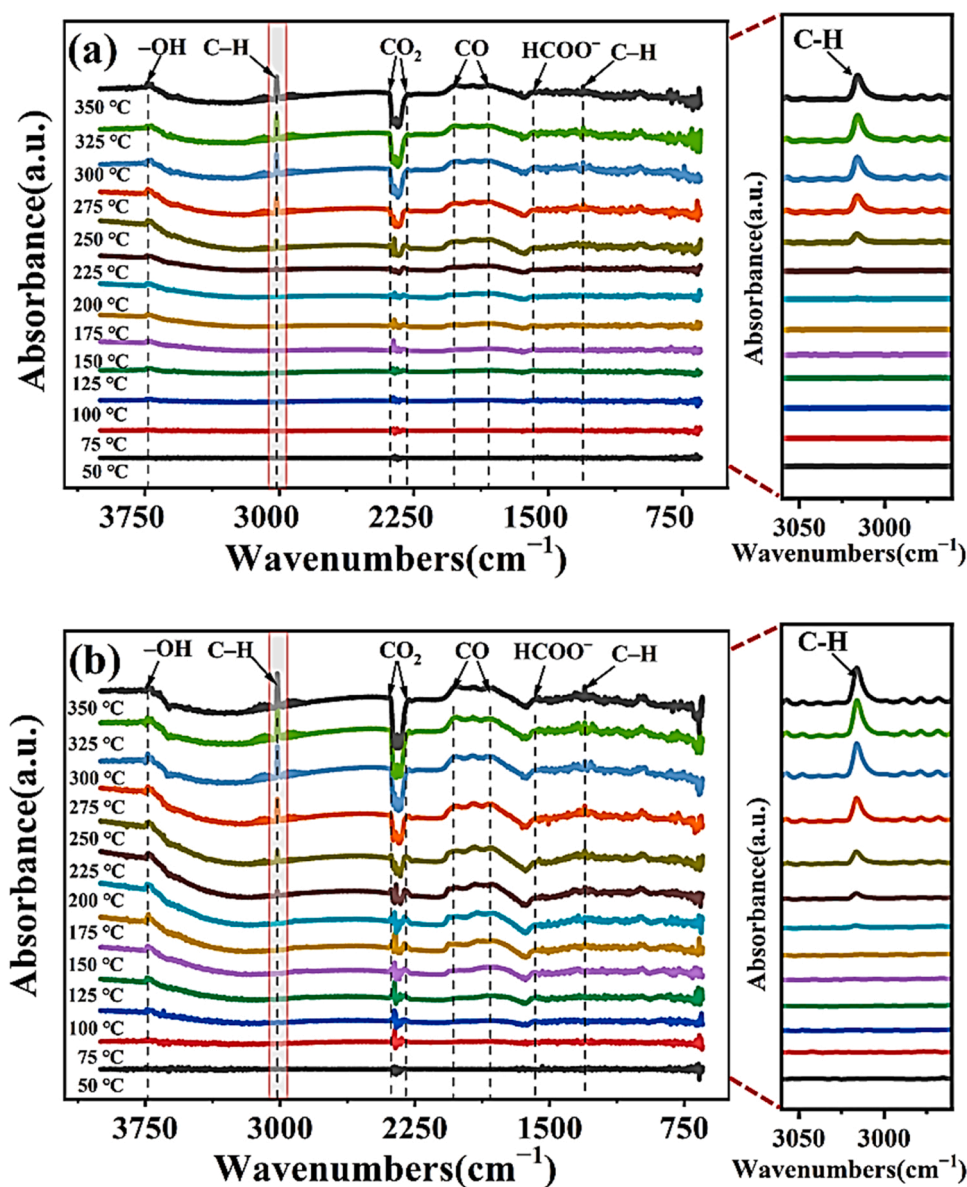
Fig. 14. *In-situ* DRIFTS analysis for CO_2 methanation of the $600^{\circ}C$-reduced catalysts: (a) Ni-NT and (b) Ni_8Mg_2-NT.

the conventional nanotubular Ni-phyllosilicate due to its solid solution structure and the special characteristics of Ni-Mg-phyllosilicate species.

CRediT authorship contribution statement

Dehui Wang: Writing – original draft, Characterization, Data curation, Validation. **Jia Liu:** Writing – original draft, Investigation, Data curation. **Hai Li:** Data curation. **Qing Liu:** Writing – review & editing, Supervision, Methodology, Project administration. **Yu Cheng:** Writing – review & editing. **Xing Fan:** Writing – review & editing. **Peng Liang:** Writing – review & editing.

Declaration of Competing Interest

The authors declare that they have no known competing financial interests or personal relationships that could have appeared to influence the work reported in this paper.

Data Availability

Data will be made available on request.

Appendix A. Supporting information

Supplementary data associated with this article can be found in the online version at doi:10.1016/j.apcatb.2023.122452.

References

[1] A.G. Olabi, M. Abdelkareem, Renewable energy and climate change, Renew. Sust. Energy Rev. 158 (2022), 112111.

[2] D. Fu, M.E. Davis, Carbon dioxide capture with zeotype materials, Chem. Soc. Rev. 51 (2022) 9340–9370.

[3] X. Zhu, W. Xie, J. Wu, Y. Miao, C. Xiang, C. Chen, B. Ge, Z. Gan, F. Yang, M. Zhang, D. O'Hare, J. Li, T. Ge, R. Wang, Recent advances in direct air capture by adsorption, Chem. Soc. Rev. 51 (2022) 6574–6651.

[4] W. Li, Y. Liu, M. Mu, F. Ding, Z. Liu, X. Guo, C. Song, Organic acid-assisted preparation of highly dispersed Co/ZrO$_2$ catalysts with superior activity for CO$_2$ methanation, Appl. Catal. B 254 (2019) 531–540.

[5] F. Dattila, R. Seemakurthi, Ye Zhou, N. Lopez, Modeling operando electrochemical CO$_2$ reduction, Chem. Rev. 122 (2022) 11085–11130.

[6] Y. Chen, Q. Liu, Synthesis and regeneration of Ni-phyllosilicate catalysts using a versatile double-accelerator method: a comprehensive study, ACS Catal. 11 (2021) 12570–12584.

[7] S. Navarro-Jaen, J.C. Navarro, L.F. Bobadilla, M.A. Centeno, O.H. Laguna, J. A. Odriozola, Size-tailored Ru nanoparticles deposited over γ-Al$_2$O$_3$ for the CO$_2$ methanation reaction, Appl. Surf. Sci. 483 (2019) 750–761.

[8] K. Wang, Y. Men, S. Liu, J. Wang, Y. Li, Y. Tang, Z. Li, W. An, X. Pan, L. Li, Decoupling the size and support/metal loadings effect of Ni/SiO$_2$ catalysts for CO$_2$ methanation, Fuel 304 (2021) 121388.

[9] J. Liu, Y. Zhang, Y. Chen, Q. Liu, Controllable synthesis of yolk–shell nickel phyllosilicate for CO$_2$ methanation: Identifying effect of pore structure of silica sacrificial template, Mater. Today Nano 18 (2022), 100208.

[10] Z. Bian, S. Kawi, Preparation, characterization and catalytic application of phyllosilicate: a review, Catal. Today 339 (2020) 3–23.

[11] B. Ma, H. Cui, D. Wang, P. Wu, C. Zhao, Controllable hydrothermal synthesis of Ni/H-BEA with a hierarchical core–shell structure and highly enhanced biomass hydrodeoxygenation performance, Nanoscale 9 (2017) 5986–5995.

[12] M. Yang, P. Jin, Y. Fan, C. Huang, N. Zhang, W. Weng, M. Chen, H. Wan, Ammonia-assisted synthesis towards a phyllosilicate-derived highly-dispersed and long-lived Ni/SiO$_2$ catalyst, Catal. Sci. Technol. 5 (2015) 5095–5099.

[13] X. Kong, Y. Zhu, H. Zheng, X. Li, Y. Zhu, Y.-W. Li, Ni nanoparticles inlaid nickel phyllosilicate as a metal–acid bifunctional catalyst for low-temperature hydrogenolysis reactions, ACS Catal. 5 (2015) 5914–5920.

[14] S. Das, J. Ashok, Z. Bian, N. Dewangan, M. Wai, Y. Du, A. Borgna, K. Hidajat, S. Kawi, Silica–Ceria sandwiched Ni core–shell catalyst for low temperature dry reforming of biogas: Coke resistance and mechanistic insights, Appl. Catal. B 230 (2018) 220–236.

[15] D. Guo, Y. Lu, Y. Ruan, Y. Zhao, Y. Zhao, S. Wang, X. Ma, Effects of extrinsic defects originating from the interfacial reaction of CeO$_{2−x}$-nickel silicate on catalytic performance in methane dry reforming, Appl. Catal. B 277 (2020), 119278.

[16] Y. Zhang, H. Duan, Z. Lv, Q. Liu, X. Wu, Which is the better catalyst for CO$_2$ methanation–Nanotubular or supported Ni-phyllosilicate?, Int. J. Hydrog, Energy 46 (2021) 39903–39911.

[17] D. Guo, Y. Lu, Y. Zhao, M. Li, Y. Zhao, S. Wang, X. Ma, Enhanced thermocatalytic stability by coupling nickel step sites with nitrogen heteroatoms for dry reforming of methane, ACS Catal. 12 (2021) 316–330.

[18] M. Fu, R. Lv, Y. Lei, M. Terrones, Ultralight flexible electrodes of nitrogen-doped carbon macrotube sponges for high-performance supercapacitors, Small 17 (2021), 2004827.

[19] F. Liu, Y.S. Park, D. Diercks, P. Kazempoor, C. Duan, Enhanced CO$_2$ methanation activity of Sm$_{0.25}$Ce$_{0.75}$O$_{2-δ}$–Ni by modulating the chelating agents-to-metal cation ratio and tuning metal–support interactions, ACS Appl. Mater. Interfaces 14 (2022) 13295–13304.

[20] F. He, J. Zhuang, B. Lu, X. Liu, J. Zhang, F. Gu, M. Zhu, J. Xu, Z. Zhong, G. Xu, Ni-based catalysts derived from Ni-Zr-Al ternary hydrotalcites show outstanding catalytic properties for low-temperature CO$_2$ methanation, Appl. Catal. B 293 (2021), 120218.

[21] J. Ashok, Z. Bian, Z. Wang, S. Kawi, Ni-phyllosilicate structure derived Ni–SiO$_2$–MgO catalysts for bi-reforming applications: acidity, basicity and thermal stability, Catal. Sci. Technol. 8 (2018) 1730–1742.

[22] F. Meshkani, M. Rezaei, Nickel catalyst supported on magnesium oxide with high surface area and plate-like shape: a highly stable and active catalyst in methane reforming with carbon dioxide, Catal. Commun. 12 (2011) 1046–1050.

[23] L. Xu, H. Song, L. Chou, Carbon dioxide reforming of methane over ordered mesoporous NiO–MgO–Al$_2$O$_3$ composite oxides, Appl. Catal. B 108 (2011) 177–190.

[24] Y. Yan, Y. Dai, H. He, Y. Yu, Y. Yang, A novel W-doped Ni-Mg mixed oxide catalyst for CO$_2$ methanation, Appl. Catal. B 196 (2016) 108–116.

[25] J.-y Jing, Z.-h Wei, Y.-b Zhang, H.-c Bai, W.-y Li, Carbon dioxide reforming of methane over MgO-promoted Ni/SiO$_2$ catalysts with tunable Ni particle size, Catal. Today 356 (2020) 589–596.

[26] X. Chen, X. Wang, S. Yao, X. Mu, Hydrogenolysis of biomass-derived sorbitol to glycols and glycerol over Ni-MgO catalysts, Catal. Commun. 39 (2013) 86–89.

[27] Y. Zhao, B. Liu, R. Amin, CO$_2$ reforming of CH$_4$ over MgO-doped Ni/MAS-24 with microporous ZSM-5 structure, Ind. Eng. Chem. Res. 55 (2016) 6931–6942.

[28] Z. Bian, I.Y. Suryawinata, S. Kawi, Highly carbon resistant multicore-shell catalyst derived from Ni-Mg phyllosilicate nanotubes@silica for dry reforming of methane, Appl. Catal. B 195 (2016) 1–8.

[29] X. Yang, M. Huang, H. Huang, D. Li, Y. Zhan, L. Jiang, Carbon dioxide methanation over Ni catalysts prepared by reduction of Ni$_x$Mg$_{3−x}$Al hydrotalcite-like compounds: Influence of Ni: Mg molar ratio, Int. J. Hydrog. Energy 47 (2022) 22442–22453.

[30] X.-Y. Yu, L. Yu, L. Shen, X. Song, H. Chen, X.W. Lou, General formation of MS (M = Ni, Cu, Mn) box-in-box hollow structures with enhanced pseudocapacitive properties, Adv. Funct. Mater. 24 (2014) 7440–7446.

[31] Y. Yang, Q. Liang, J. Li, Y. Zhuang, Y. He, B. Bai, X. Wang, Ni$_3$Si$_2$O$_5$(OH)$_4$ multi-walled nanotubes with tunable magnetic properties and their application as anode materials for lithium batteries, Nano Res. 4 (2011) 882–890.

[32] J. Lian, C. Zhang, P. Wang, D.H. Ng, Template-free hydrothermal synthesis of mesoporous MgO nanostructures and their applications in water treatment, Chem. Asian J. 7 (2012) 2650–2655.

[33] R.D. White, D.V. Bavykin, F.C. Walsh, Morphological control of synthetic Ni$_3$Si$_2$O$_5$(OH)$_4$ nanotubes in an alkaline hydrothermal environment, J. Mater. Chem. A 1 (2013) 548–556.

[34] L. Shen, J. Xu, M. Zhu, Y.-F. Han, Essential role of the support for nickel-based CO$_2$ methanation catalysts, ACS Catal. 10 (2020) 14581–14591.

[35] L. Liu, H. Lou, M. Chen, Selective hydrogenation of furfural to tetrahydrofurfuryl alcohol over Ni/CNTs and bimetallic CuNi/CNTs catalysts, Int. J. Hydrog. Energy 41 (2016) 14721–14731.

[36] J. Liu, C. Li, F. Wang, S. He, H. Chen, Y. Zhao, M. Wei, D.G. Evans, X. Duan, Enhanced low-temperature activity of CO$_2$ methanation over highly-dispersed Ni/TiO$_2$ catalyst, Catal. Sci. Technol. 3 (2013) 2627–2633.

[37] L. Li, L. Song, H. Wang, C. Chen, Y. She, Y. Zhan, X. Lin, Q. Zheng, Water-gas shift reaction over CuO/CeO$_2$ catalysts: Effect of CeO$_2$ supports previously prepared by precipitation with different precipitants, Int. J. Hydrog. Energy 36 (2011) 8839–8849.

[38] J. Liu, H. Peng, W. Liu, X. Xu, X. Wang, C. Li, W. Zhou, P. Yuan, X. Chen, W. Zhang, Tin modification on Ni/Al$_2$O$_3$: Designing potent coke-resistant catalysts for the dry reforming of methane, ChemCatChem 6 (2014) 2095–2104.

[39] Q. Liu, J. Gao, F. Gu, X. Lu, Y. Liu, H. Li, Z. Zhong, B. Liu, G. Xu, F. Su, One-pot synthesis of ordered mesoporous Ni–V–Al catalysts for CO methanation, J. Catal. 326 (2015) 127–138.

[40] R. Lü, J. Lin, Z. Qu, Theoretical study on interactions between ionic liquids and organosulfur compounds, Comput. Theor. Chem. 1002 (2012) 49–58.

[41] C. Lv, L. Xu, M. Chen, Y. Cui, X. Wen, C.-e Wu, B. Yang, F. Wang, Z. Miao, X. Hu, Q. Shou, Constructing highly dispersed Ni based catalysts supported on fibrous silica nanosphere for low-temperature CO$_2$ methanation, Fuel 278 (2020), 118333.

[42] Z. Zhang, X. Zhang, J. Zhang, J. Gao, Y. Shao, D. Dong, S. Zhang, Q. Liu, L. Xu, X. Hu, Impacts of alkali or alkaline earth metals addition on reaction intermediates formed in methanation of CO$_2$ over cobalt catalysts, J. Energy Inst. 93 (2020) 1581–1596.

[43] J. Liu, W. Bing, X. Xue, F. Wang, B. Wang, S. He, Y. Zhang, M. Wei, Alkaline-assisted Ni nanocatalysts with largely enhanced low-temperature activity toward CO$_2$ methanation, Catal. Sci. Technol. 6 (2016) 3976–3983.

[44] H. Muroyama, Y. Tsuda, T. Asakoshi, H. Masitah, T. Okanishi, T. Matsui, K. Eguchi, Carbon dioxide methanation over Ni catalysts supported on various metal oxides, J. Catal. 343 (2016) 178–184.

[45] H. Takano, Y. Kirihata, K. Izumiya, N. Kumagai, H. Habazaki, K. Hashimoto, Highly active Ni/Y-doped ZrO$_2$ catalysts for CO$_2$ methanation, Appl. Surf. Sci. 388 (2016) 653–663.